
ADA-DPM: A NEURAL DESCRIPTORS-BASED ADAPTIVE NOISE POINT FILTERING STRATEGY FOR SLAM

A PREPRINT

 **Yongxin Shao**

College of Metrology Measurement and Instrument
China Jiliang University
Hangzhou, China 031100
shaoyxpaper@163.com

Binrui Wang*

College of Mechanical and Electrical Engineering
China Jiliang University
Hangzhou, China 031100
wangbrpaper@163.com

 **Aihong Tan**

College of Mechanical and Electrical Engineering
China Jiliang University
Hangzhou, China 031100
Tanah@cjlu.edu.cn

June 24, 2025

ABSTRACT

LiDAR SLAM has demonstrated significant application value in various fields, including mobile robot navigation and high-precision map construction. However, existing methods often need to make a trade-off between positioning accuracy and system robustness when faced with dynamic object interference, point cloud noise, and unstructured environments. To address this challenge, we propose an adaptive noise filtering SLAM strategy—ADA-DPM, achieving excellent preference in both aspects. We design the Dynamic Segmentation Head to predict the category of feature points belonging to dynamic points, to eliminate dynamic feature points; design the Global Importance Scoring Head to adaptively select feature points with higher contribution and features while suppressing noise interference; and construct the Cross Layer Intra-Graph Convolution Module (GLI-GCN) to fuse multi-scale neighborhood structures, thereby enhancing the discriminative ability of overlapping features. Finally, to further validate the effectiveness of our method, we tested it on several publicly available datasets and achieved outstanding results.

Keywords SLAM · Deep Learning · LiDAR · Point Cloud

1 Introduction

Autonomous mobile robots are playing an increasingly important role in today’s society, with their application scope gradually expanding and covering a wide range of fields. This expansion is of great significance for improving work efficiency, addressing challenges faced by humanity, and promoting technological innovation [1–4]. SLAM (Simultaneous Localization and Mapping) is a fundamental issue in robotic environmental perception. The goal is to construct a spatial map and determine real-time location information while the robot moves in an unknown envi-

ronment, without prior knowledge, using the sensors it carries [5].

Visual SLAM has been widely used in platforms with strict payload requirements such as drones and robots [6–8], benefiting from the advantages of cameras like small size, light weight, simple installation, and low cost. However, cameras exhibit poor accuracy and robustness in scenarios with abrupt light changes or lack of texture features. Compared with cameras [9, 10], LiDAR can more effectively preserve the structural information of the environment in the collected data, and it is not affected by ambient light, making it more stable and reliable in complex environments. This has made LiDAR SLAM one of the hot research directions attracting extensive attention from many scholars at present [11].

This work has been submitted to the IEEE for possible publication. Copyright may be transferred without notice, after which this version may no longer be accessible.

Currently, LiDAR SLAM can be categorized into two types based on feature extraction methods: handcrafted feature-based SLAM and deep learning-based SLAM. The former [12–14] typically relies on geometric rules (e.g., corner features, plane features) to design features. However, since it cannot comprehend the semantic information of the environment, it often faces issues such as feature sparsity or redundancy. In low-texture scenes (such as tunnels, grasslands, etc.), geometric features are often sparse, making it easy to lose key constraints and leading to pose estimation drift. While dense features can increase the number of features, they impose high computational overhead and memory consumption, making it difficult to support real-time reconstruction of large-scale scenes. In contrast, deep learning-based methods [15, 16] can achieve more accurate global registration and predict the probability of loop closure existence by extracting more compact features, thereby efficiently completing robot localization and mapping tasks.

However, in some complex scenarios (such as scenes lacking fixed landmarks like buildings or roads, terrains with hills and ravines, or scenes with numerous dynamic objects), dynamic objects (e.g., pedestrians, vehicles) and anomalies in the LiDAR data can severely contaminate feature matching. Specifically, for scenes with numerous dynamic objects, SLAM algorithms generally exhibit a certain level of robustness, where a small number of dynamic targets can be adapted during registration. However, once the proportion of dynamic objects in the scene becomes too high, the ego-motion of dynamic objects introduces additional local constraints, leading to a decline in trajectory accuracy and even complete failure of the trajectory. For complex, unstructured environments, LiDAR point cloud often contains significant noise and outliers, which can affect local feature extraction and cause incorrect feature point matching, ultimately leading to erroneous pose estimation. Secondly, existing algorithms often overlook the heterogeneity in feature point importance, assigning them uniform significance a priori. In SLAM tasks, not all feature points are equally important. Compared with irregularly distributed unstructured feature points (such as those from vegetation), regularly distributed feature points (from structures like buildings and road signs) are more conducive to correct feature matching.

What’s more, existing deep learning-based SLAM methods often face issues such as limited receptive fields and low feature extraction resolution, overlooking the importance of perceiving neighborhood structures at multiple scales. This is particularly problematic in loop closure detection tasks, where certain overlapping regions in the point cloud may experience a significant reduction in similarity as the receptive field increases, leading to incorrect predictions of repetitive scenes and, ultimately, errors in pose estimation.

To address the aforementioned issues, we design an adaptive noise-filtering SLAM strategy, ADA-DPM.

To handle the interference from dynamic objects, we propose a Dynamic Point Prediction Module (Dynamic Seg-

mentation Head). Specifically, we constructed the Dynamic Segmentation Head to predict the category of feature points (whether they belong to dynamic points or static points), removing feature points predicted as dynamic points in order to eliminate the disturbance caused by dynamic objects’ ego-motion on global pose prediction.

To address the interference of outliers and unstructured feature points, we propose the Global Importance Scoring Module (Importance Scoring Head). Specifically, we assign an importance score to each paired feature point, highlighting those that are reliable and contribute to registration while filtering out low-importance points (which may be noise, outliers, or unstructured feature points), thereby further improving the accuracy of feature point pairing. To supervise the prediction of global importance scores, we designed a global reconstruction loss weighted by importance scores. We use the global rigid transformation directly predicted by the KAN Linear Layer [17] to align feature points, and weight the reconstruction errors with importance scores, where the importance of current feature point pairs is measured by the reconstruction errors. Additionally, we constructed a scoring loss with all-ones labels to prevent the network from reducing the global reconstruction loss by predicting all-zero importance scores as a trivial solution during the training phase. This design explicitly avoids the degenerate scenario where the network circumvents meaningful feature selection by assigning uniform zero weights, ensuring the training process prioritizes non-trivial importance estimation. Finally, by supervising the prediction of global rigid transformations between feature points, implicit supervision is applied to the feature extraction network, enabling the network to learn to extract feature points that are more contributory to the point cloud registration task.

To alleviate the reduction in similarity of overlapping regions caused by low resolution, we designed the GLI-GCN (Cross Layer Intra-Graph Convolution) module. Specifically, through cross-layer feature point sampling, we collect the neighborhood features of deep-layer feature points corresponding to those in shallow layers, and construct a local neighborhood graph to perceive neighborhood structures at different scales and capture richer geometric features.

In summary, the main contributions of this paper are as follows:

- We designed an adaptive noise point filtering strategy, where the Dynamic Segmentation Head predicts the category of feature points and removes those predicted as dynamic points. Additionally, the Importance Scoring Head assigns importance scores to feature point pairs, removing erroneous matches caused by outliers.
- We designed the GLI-GCN module, which uses neighborhoods with different receptive fields to generate local feature descriptors that integrate multiple receptive fields, addressing the problem

where the similarity of overlapping region neighborhood structures is reduced due to a single receptive field.

- To highlight the advantages of our method, we conducted experimental validation on multiple datasets and further verified the robustness against point cloud noise on datasets with added noise. Experimental results show that our method achieves good positioning accuracy and demonstrates strong robustness to noisy points.

2 Related Work

The foundation of SLAM lies in the matching of relevant feature points between consecutive frame point clouds. Based on the encoding methods of point cloud feature, it can be divided into handcrafted feature-based methods and deep learning-based methods.

2.1 Handcrafted Feature-based Methods

Hand-crafted feature methods generally rely on traditional geometric algorithms to extract structured features such as lines, planes, and corner points from point clouds, enabling matching of relevant feature points between adjacent frames. Besl et al. proposed a method based on Iterated Closest Points (ICP) [18], which laid the foundation for inter-frame matching in SLAM. Although widely applied, ICP is prone to local optima. To address this, [13] proposed PLICP, modifying traditional ICP by changing the point-to-point distance to the distance from a point to the line connecting its two nearest points. NICP [13] presents an online recursive point cloud alignment approach, determining corresponding data using the 3D structure around points and minimizing errors based on normal vector and curvature features via least squares. Deschaud et al. [14] proposed IMLSICP, a low-drift algorithm for 3D LiDAR point clouds, which employs a specific sampling strategy to select representative LiDAR points and minimize their distance to the model point cloud. Yang et al. [12] integrated the branch and bound method to enable effective 3D space search. Although the above ICP-based methods address the local optima issue of ICP, they suffer from a severe lack of matching points in large-scale sparse point clouds, leading to low positioning accuracy. To tackle this problem, Segal et al. proposed a generalized ICP method based on point-to-plane distance [19], and Zhang Ji et al. combined this approach with point-to-edge distance to introduce the renowned LOAM [20] framework. Subsequent variants of LOAM, such as LeGO-LOAM [21] and LOAM linux [22], were then developed. These schemes demonstrate favorable performance in texture-rich structured scenes, but they remain constrained by the LiDAR field of view and environmental structural features [23].

2.2 Deep Learning-Based Methods

Deep learning-based methods generally leverage neural networks (such as PointNet [24], PointNet++ [25], etc.) to automatically learn the global semantic features and contextual relationships of point clouds for feature point matching between adjacent frames. Unlike hand-crafted feature methods, deep learning solutions provide an alternative data-driven approach, eschewing the need to create hand-crafted algorithms via physical models or geometric theories. DCP [15] employs soft matching alignment based on singular value decomposition (SVD) to efficiently estimate rigid transformations between adjacent frame point clouds. Building on this design, PRNet [26] embeds a key-point detection module to enable the registration network to handle partial overlapping point cloud registration, and improves the soft matching in DCP to hard matching using the Gumbel-softmax operator, further enhancing registration accuracy. RPMNet [26] utilizes hand-crafted feature descriptors to fully exploit the local geometric structure information of point clouds, combining it with deep feature learning to construct robust point feature representations. To more effectively suppress outlier interference, it introduces doubly stochastic constraints into the learned soft matching matrix to evaluate the inlier confidence of matching pairs and filter outliers, achieving robust rigid transformation estimation under partial overlap. Furthermore, by deeply fusing spatial geometric and depth feature information, IDAM [27] constructs a distance-aware soft matching matrix to enhance the robustness of point correspondence matching. RGM [28] leverages graph matching algorithms to fuse node and edge information of point clouds for discriminative point pair matching, and estimates rigid transformations by solving graph matching optimization via Sinkhorn iterations.

PointNetLK [29] employs PointNet [24] for global feature extraction and modifies the Lucas-Kanade algorithm to circumvent the inherent limitation that PointNet representations cannot undergo gradient estimation via convolution. However, since PointNet fails to aggregate information from both point clouds, it is sensitive to partially visible point clouds. The method iteratively optimizes the feature distance between point clouds using a differentiable Lucas-Kanade algorithm to solve for rigid transformations. RegTR [30] leverages the powerful feature representation capability of Transformer to achieve end-to-end point cloud registration at large-scale scene levels. OMNet [16] learns an overlapping region mask to remove non-overlapping areas, thereby extracting discriminative global point cloud features for iterative point cloud registration. UTOPIC [31] explicitly models the uncertainty of overlapping region masks, enabling the model to better handle ambiguous predictions of overlapping regions between point clouds and improving its reliability in complex scenarios. FINet [32] proposes a dual-branch rigid transformation regression model, decoupling rotation and translation features at the feature level to achieve robust transformation estimation. DeepMapPoint [33] uses neural networks to extract highly representative and sparse neural

descriptors from point clouds, enabling memory-efficient map representation and accurate multi-scale positioning tasks (e.g., odometry and loop closure), thus constructing a fully deep learning-based SLAM framework.

Early SLAM research often relied on the assumption of fully static scenes for simplification, but dynamic and semi-dynamic objects are inevitable in real environments, imposing adverse effects on SLAM. To address this, Ruchti et al. [34] compute the probability of dynamic objects in each frame via a network and filter out those with high probabilities. RangeNet++ [35] converts point clouds into depth maps for semantic segmentation, then reconstructs maps using semantically annotated points. Pfreundschuh et al. [36] directly employ a point cloud segmentation network to segment raw point clouds, filtering out dynamic points before the mapping process. Although these methods mitigate dynamic object interference to some extent, they typically require auxiliary networks, adding extra computational overhead.

3 Methodology

3.1 Problem Definition

The core objective of LiDAR SLAM is to incrementally construct an environmental map in real-time and simultaneously localize the sensor itself using continuous frames of LiDAR observation data. The essence of this problem can be reduced to dynamic pose estimation optimization, that is, solving the sensor’s motion trajectory by frame-by-frame point cloud registration in an unknown environment. Its mathematical formulation can be expressed as finding the optimal rigid transformation parameters that align consecutive frame point clouds in spatial consistency after transformation. Specifically, let the source point cloud of the k -th frame be $\mathcal{X} = \{x_i \in \mathbb{R}^3\}_{i=1}^N$, and the historical point cloud map be $\mathcal{Y} = \{y_j \in \mathbb{R}^3\}_{j=1}^M$. The pose transformation to be solved, $\mathcal{T} = \{\mathcal{R}, t\}$, includes the rotation matrix $\mathcal{R} \in SO(3)$ and the translation vector $t \in \mathbb{R}^3$. The objective function to be solved can be expressed as:

$$\min_{\mathcal{R}, t} \sum_{x_i, y_j \in C} \|\mathcal{R}x_i + t - y_j\|_2 \quad (1)$$

where C represents the set of potential correspondences between the two point clouds, and $\|\cdot\|_2$ is the Euclidean distance. Due to the presence of observation noise, dynamic objects, and outliers in real-world scenarios, the true correspondences C cannot be directly obtained, which causes traditional SLAM algorithms to easily fall into local optima. Therefore, the focus of this paper is on how to avoid interference from dynamic objects and outliers, establish accurate point correspondences, and design noise-robust optimization strategies to improve the accuracy and robustness of the LiDAR SLAM system.

3.2 SLAM System

The specific process of ADA-DPM is shown in Figure 1, which mainly consists of three stages: Odometry, Loop-Closure Detection, and Pose Graph Optimization.

Odometry: The Odometry stage predicts the optimal rigid transformation \mathcal{T} between the current frame’s point cloud and the historical keyframes to obtain the initial pose. The specific process is shown in the green part of Figure 1, where \mathcal{P}_i represents the point cloud set at the i -th moment, \mathcal{P} represents the historical point clouds up to the $(i-1)$ -th moment, and \mathcal{K} represents the historical keyframe point cloud set. First, we use KNN (K-Nearest Neighbor) to compute the nearest keyframe point cloud \mathcal{K}_m from the historical point cloud set \mathcal{P} (i.e., the closest keyframe point cloud in the historical keyframe set \mathcal{K} to \mathcal{P}_i), which is taken as the source point cloud \mathcal{P}_{src} . Using point cloud registration, we predict the rigid transformation \mathcal{T}_i between the source point cloud \mathcal{P}_{src} and the target point cloud \mathcal{P}_i , and add \mathcal{T}_i and the point cloud \mathcal{P}_i to the pose graph for subsequent pose graph optimization.

In addition, during Odometry, we also determine whether the current frame’s point cloud should be added to the historical keyframe set \mathcal{K} . Firstly, we use the predicted rigid transformation \mathcal{T}_i to transform the feature point pairs matched between the source point cloud \mathcal{P}_{src} and the i -th frame’s point cloud \mathcal{P}_i into the same coordinate system. We then compute the RMSE (Root Mean Square Error) between the transformed point clouds. If the RMSE (as shown in (2)) is below a certain threshold and the matching confidence τ (mathematical representation of matching confidence as shown in (3) and (4)) is above a certain threshold, \mathcal{P}_i will be considered as a candidate keyframe. To avoid the burden caused by frequent keyframe insertion in subsequent calculations, we compute the minimum Euclidean distance between \mathcal{P}_i and the historical keyframes in set \mathcal{K} , and only if this distance exceeds a certain threshold will \mathcal{P}_i be inserted into the historical keyframe set \mathcal{K} . It is worth noting that in the initial stage of SLAM, the pose of the first frame’s point cloud is initialized as the identity matrix, and this frame’s point cloud is set as the first keyframe.

$$RMSE = \sqrt{\frac{1}{n} \sum_{i=1}^n \left[\hat{\mathcal{P}}_i - \left(\mathcal{R}_i \hat{\mathcal{P}}_{src} + t_i \right) \right]} \quad (2)$$

where $\hat{\mathcal{P}}_{src}$ and $\hat{\mathcal{P}}_i$ represent the feature points paired between the source point cloud \mathcal{P}_{src} and the target point cloud \mathcal{P}_i ; $\mathcal{R}_i \in SO(3)$ and $t_i \in \mathbb{R}^3$ are the rotation and translation components of the rigid transformation \mathcal{T}_i between the source point cloud \mathcal{P}_{src} and the target point cloud \mathcal{P}_i .

Loop-Closure Detection: The Loop-Closure Detection stage corrects the global trajectory and map by predicting whether there exists a loop closure between the i -th frame point cloud \mathcal{P}_i and the historical keyframe point cloud set \mathcal{K} . The specific process is shown in the blue part

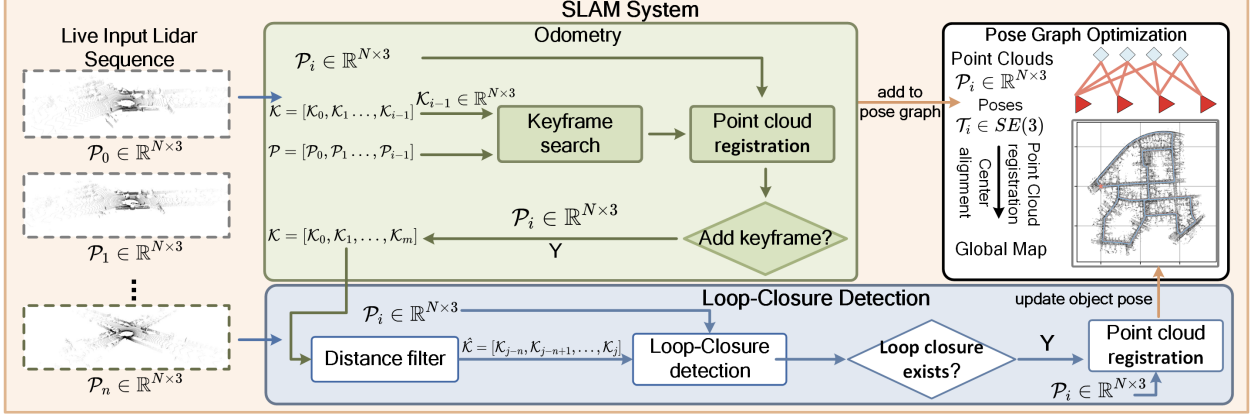


Figure 1: Overview of the SLAM system process. The green part represents the odometry part; the blue part represents loop closure detection; the white part represents pose graph optimization; and the blue-boxed portion within the white part represents the final global map and trajectory obtained.

of Figure 1. Firstly, we compute the Euclidean distance between \mathcal{P}_i and \mathcal{K} , and find the set of loop closure candidate keyframes within a certain distance threshold relative to \mathcal{P}_i . Then, the relative transformation pose between \mathcal{P}_i and the candidate keyframe set is computed, and keyframes with small transformation magnitudes are excluded to obtain the loop closure keyframe set $\hat{\mathcal{K}} = [\mathcal{K}_{j-n}, \mathcal{K}_{j-n+1}, \dots, \mathcal{K}_j]$. Next, the probability of a loop closure between \mathcal{P}_i and the loop closure keyframes $\hat{\mathcal{K}}$ is predicted, and the top K frames with the highest probability are selected as the new loop closure point cloud set $\hat{\mathcal{K}}$. Finally, the transformation pose between the predicted loop closure point cloud set $\hat{\mathcal{K}}$ and \mathcal{P}_i is estimated using point cloud registration, and the predicted pose is updated in the pose graph. It's important to note that to avoid frequent Loop-Closure Detection, Loop-Closure Detection is only performed when a certain number of keyframes have been accumulated.

Pose-Graph Optimization: The Pose-Graph Optimization stage corrects the drift in the trajectory and map by merging historical observation data and utilizing global constraints. The specific process is shown in the white part of Figure 1. First, we use KNN to compute the k nearest point clouds to the most recent keyframe point cloud \mathcal{K}_m in the historical point cloud set \mathcal{P} , and by calculating their Euclidean distance to v , we exclude point clouds that exceed a certain distance threshold, thus obtaining the neighboring frames of \mathcal{P}_i in the pose graph. Then, the relative transformation pose between the neighboring frames of \mathcal{P}_i is computed, and the frames are transformed into the same coordinate system to obtain the local map. Using point cloud registration, the rigid transformation between \mathcal{P}_i and the local map is computed to optimize the pose in the pose graph. Finally, graph optimization is applied to optimize the pose graph, yielding the final rigid transformation (using the standard pose graph optimization provided in Open3D [37]).

3.3 Point Cloud Registration

The network structure of ADA-DPM is shown in Figure 2, which mainly consists of two parts: (1) Encoder: the Encoder extracts features from the input source point cloud \mathcal{P}_{src} and target point cloud \mathcal{P}_{dst} to obtain the sparse feature descriptor of the point cloud $[\bar{\mathcal{P}}, \bar{\mathcal{F}}] \in \mathbb{R}^{N \times (M+3)}$; (2) Decoder: the Decoder predicts the rigid transformation between the descriptors of the two frames of point clouds and the probability that a loop exists between them.

Encoder: The Encoder part, as shown in the blue part of Figure 2, uses sparse point cloud descriptors containing compressed feature information to represent the complex point clouds captured by LiDAR. Specifically, the point cloud captured by LiDAR can be represented as a set of 3D coordinates $\mathcal{P} = [p_1, p_2, \dots, p_n] \in \mathbb{R}^3$. ADA-DPM feeds the source point cloud \mathcal{P}_{src} and the target point cloud \mathcal{P}_{dst} into a weight-shared feature extraction structure to obtain sparse compressed point cloud descriptors. The feature extraction network is shown in the blue part of Figure 2, consisting of PointNeXt [38] and CLI-GCN (as described in Section D in chapter 3). Firstly, PointNeXt is used to downsample the complex point clouds and aggregate their neighboring set features. Then, CLI-GCN is used to aggregate local geometric features at different scales across the receptive field to enrich the structural information of the point clouds. Finally, the compressed descriptors of the source and target point clouds are obtained: $[\bar{\mathcal{P}}_{src}, \bar{\mathcal{F}}_{src}] \in \mathbb{R}^{N \times (C+3)}$, $[\bar{\mathcal{P}}_{dst}, \bar{\mathcal{F}}_{dst}] \in \mathbb{R}^{N \times (C+3)}$.

Decoder: The Decoder part, as shown in the white part of Figure 2, mainly consists of the feature attention fusion module for the previous and current frames, as well as various decoding heads.

Feature Attention Fusion Module: The feature attention fusion module for the previous and current frames consists of self-attention module, cross-attention module, and MLP (Multilayer Perceptron): (1) the self-attention module inte-

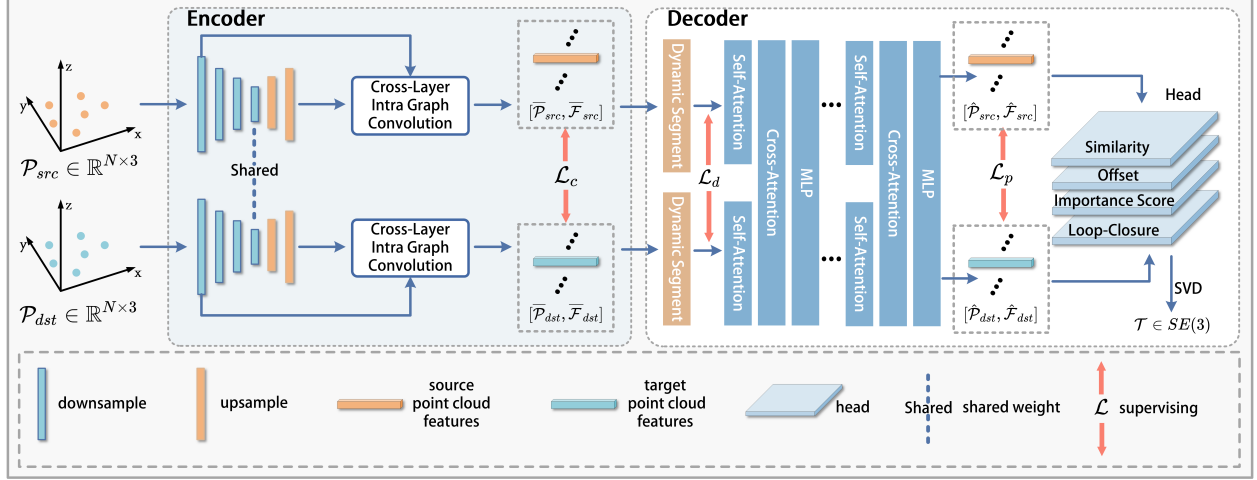


Figure 2: Overview of the network architecture. The blue part represents the Encoder, and the white part represents the Decoder. The networks for both the source point cloud and the target point cloud share the same weights.

grates the global features of the compressed point cloud descriptors of the source and target point clouds encoded by the Encoder; (2) the cross-attention module exchanges the contextual information between the source and target point clouds; (3) the MLP integrates the feature information. The final output is the decoded compressed point cloud descriptors: $[\hat{\mathcal{P}}_{src}, \hat{\mathcal{F}}_{src}] \in \mathbb{R}^{N \times (C+3)}$, $[\hat{\mathcal{P}}_{dst}, \hat{\mathcal{F}}_{dst}] \in \mathbb{R}^{N \times (C+3)}$.

Decode Heads: The decode heads mainly consist of the Similarity Head, Offset Head, Importance Scoring Head, Dynamic Segmentation Head, SVD solver, and Loop-Closure Head. Among these, the point cloud registration process involves the Similarity Head, Offset Head, Dynamic Segmentation Head, Importance Scoring Head, and SVD solver (the Loop-Closure Head is introduced in Section 3.3). (1) For the Similarity Head and Offset Head, ADA-DPM follows the strategy from DeepPointMap [33]. The Similarity Head performs feature point pair matching by evaluating the feature similarity between the compressed descriptors of the source and target point clouds (the mathematical description of the matching method is given in (3) and (4)) and predicts the matching confidence. The Offset Head predicts the offset between the matched compressed descriptors of the source and target point clouds, eliminating the misalignment in the global coordinate system. (2) The Dynamic Segmentation Head predicts the dynamic points present in the compressed descriptors and removes the interference from moving objects during point cloud registration. (3) The Importance Scoring Head provides an initial estimation of the rigid transformation between the source and target point clouds and assigns contribution scores to the matched feature point pairs, discarding those with low contribution scores. (4) Finally, the matched point pairs are used to calculate the rigid transformation between the source and target point

clouds using SVD.

$$\mathcal{M}_s = [(\|\mathcal{F}_{src}\|_c)^T @ (\|\mathcal{F}_{dst}\|_r)] \quad (3)$$

$$\tau = \text{TopK}_r [\text{Softmax}_r(\mathcal{M}_s) \odot \text{Softmax}_c(\mathcal{M}_s)] \quad (4)$$

$$[\tilde{\mathcal{P}}_{src}, \tilde{\mathcal{P}}_{dst}] = [\mathcal{P}_i^{src}, f_{\tau \rightarrow j}(\mathcal{P}_{dst})] \quad (5)$$

where $\|\cdot\|_c$ and $\|\cdot\|_r$ represent row L2 normalization and column L2 normalization, respectively; $@$ denotes matrix multiplication; \mathcal{F}_{src} and \mathcal{F}_{dst} represent the features obtained by concatenating $[\hat{\mathcal{P}}_{src}, \hat{\mathcal{F}}_{src}]$ and $[\hat{\mathcal{P}}_{dst}, \hat{\mathcal{F}}_{dst}]$ along the feature dimension; \mathcal{M}_s represents the correlation matrix between the source and target point cloud compressed descriptors; $\text{Softmax}_r(\cdot)$ and $\text{Softmax}_c(\cdot)$ denote Softmax operations applied along rows and columns, respectively; $\text{TopK}_r(\cdot)$ denotes the extraction of the maximum value from each row; \odot represents element-wise multiplication; τ denotes the confidence of matching between the source and target point cloud compressed descriptors; $f_{\tau \rightarrow j}(\cdot)$ is the mapping function that extracts the corresponding target point cloud compressed descriptor from $\tilde{\mathcal{P}}_{dst}$ based on the matching confidence with the source point cloud compressed descriptor; and $[\tilde{\mathcal{P}}_{dst}, \tilde{\mathcal{F}}_{dst}]$ represents the matched pairs of source and target point cloud compressed descriptors.

Dynamic Segmentation Head: One of the core tasks of SLAM is point cloud registration, which aims to compute the rigid transformation $\mathcal{T} \in SE(3)$ between consecutive frame point clouds using static points in the scene. However, in real-world environments (especially outdoor scenes), dynamic points, such as those belonging to pedestrians and vehicles, can interfere with the registration task due to their own ego-motion. Therefore, we constructed the Dynamic Segmentation Head to predict the category of the compressed descriptors (whether they belong to dynamic points or static points), and discard the descriptors predicted as dynamic points to remove the interference

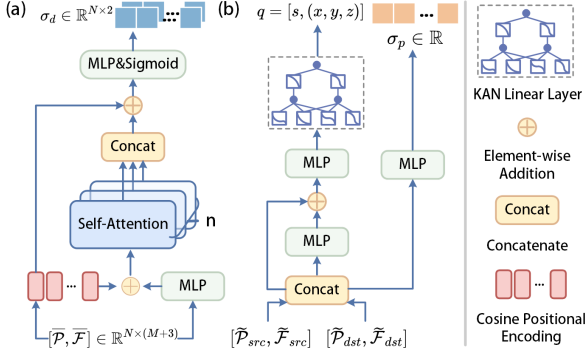


Figure 3: Overview of Dynamic Segmentation Head and Importance Scoring Head. (a) is the overview of Dynamic Segmentation Head; (b) is the overview of Importance Scoring Head.

caused by dynamic point’s ego-motion. The structure of the Dynamic Segmentation Head is shown in Figure 3(a). The Dynamic Segmentation Head utilizes a simple stack of multi-head self-attention mechanisms to deeply mine the global information of the compressed descriptors, and then uses the final MLP & Sigmoid layers to predict the probability $\sigma_d \in \mathbb{R}^{N \times 2}$ that the compressed descriptor $[\tilde{\mathcal{P}}, \tilde{\mathcal{F}}]$ belongs to dynamic points or static points.

In addition, considering that, unlike images, LiDAR point clouds lack semantic information and contain many hard-to-classify negative samples, we employ a hard-negative mining training strategy. We simultaneously predict the probabilities of being dynamic or static points, and based on the probability predicted as static points, we select the K static points with the smallest predicted probabilities (to avoid class imbalance during training, K can be up to three times the number of dynamic points) and include them in the loss function to optimize the model’s ability to distinguish between dynamic and static points.

Importance Scoring Head: Point clouds often contain a large number of noisy points and outliers, which can lead to erroneous pairings between the compressed descriptors of the source and target point clouds, interfering with the objective function for pose estimation and causing inaccurate registration. Moreover, for SLAM tasks, structural feature points (such as buildings, road signs, etc., which have regular set features) are more important than non-structural feature points (such as vegetation, which has irregular distribution). Therefore, we construct the Importance Scoring Head to assign a weight to each point, emphasizing those that are reliable and contribute to registration, assigning low weights and ignoring low-importance points (which may be noise, outliers, or edge points) to eliminate incorrect pairings of compressed descriptors.

The structure of the Importance Scoring Head is shown in Figure 3(b). It predicts the rigid transformation between $[\tilde{\mathcal{P}}_{src}, \tilde{\mathcal{P}}_{dst}]$ and scores the pairing result $\sigma_p \in \mathbb{R}$ using a stacked MLP and KAN Linear Layer [17], thus removing

those compressed descriptor pairs with lower scores. We treat the preliminary estimate of the rigid transformation between $[\tilde{\mathcal{P}}_{src}, \tilde{\mathcal{P}}_{dst}]$ as a regression task, where the rigid transformation between the source and target point clouds is predicted by decoding their features. Although MLPs are widely used for feature decoding, Sitzmann et al. [39] pointed out that the discontinuous activation functions in MLPs make it difficult to capture high-frequency information. Moreover, since the rigid transformation between the source and target point clouds must satisfy strict mathematical constraints, we use the KAN Linear Layer as a decoder (the mathematical representation of KAN Linear Layer is given by (6) and (7)) to predict the preliminary rigid transformation by learning the coefficients of continuous functions.

$$\Phi(x_i) = \begin{bmatrix} \phi_{i,1,1}(\cdot) & \phi_{i,1,2}(\cdot) & \cdots & \phi_{i,1,j}(\cdot) \\ \phi_{i,2,1}(\cdot) & \phi_{i,2,2}(\cdot) & \cdots & \phi_{i,2,j}(\cdot) \\ \vdots & \vdots & \ddots & \vdots \\ \phi_{i,k,1}(\cdot) & \phi_{i,k,2}(\cdot) & \cdots & \phi_{i,k,j}(\cdot) \end{bmatrix} \quad (6)$$

$$\text{KAN}(x) = (\Phi_{n-1} \cdot \Phi_{n-2} \cdots \Phi_1 \cdot \Phi_0)(x) \quad (7)$$

where $\phi_{(i,1,1)}(\cdot)$ represents the activation function connecting the i -th neuron at the 1-th layer and the j -th neuron at the j -th layer. $\Phi(x_i)$ is the function matrix of a KAN layer.

It should be noted that, considering that directly predicting the rigid transformation $\mathcal{T} \in SE(3)$ between $[\tilde{\mathcal{P}}_{src}, \tilde{\mathcal{P}}_{dst}]$ requires 12 variables to be predicted, in order to reduce the difficulty of the loss function’s convergence, we only predict the rotation transformation and represent the rotation using a quaternion $q = [s, (x, y, z)]$, where s is the real part of q , and x, y, z are the imaginary parts. For the translation transformation, when q is predicted accurately, after aligning the source and target point cloud descriptors using q , the difference in the coordinates of the two centers gives the translation vector (mathematically expressed as shown in (8)). In addition, by supervising the prediction of the global rigid transformation between feature points, implicit supervision can be imposed on the feature extraction network, enabling the network to learn to extract feature points that contribute more to the point cloud registration task.

$$\tilde{t} = \frac{q}{\|q\|} \tilde{\mathcal{P}}_{src}^{ctr} \left(\frac{q}{\|q\|} \right)^{-1} - \tilde{\mathcal{P}}_{dst}^{ctr} \quad (8)$$

where $(\cdot)^{-1}$ denotes the inverse of q , $\|q\|$ represents the norm of q , and $\tilde{\mathcal{P}}_{src}^{ctr}, \tilde{\mathcal{P}}_{dst}^{ctr}$ represent the center point coordinates of \mathcal{P}_{src}^{ctr} and \mathcal{P}_{dst}^{ctr} , respectively.

In order to make σ_p as accurate as possible in representing the pairing of compressed descriptors, we designed a loss function \mathcal{L}_s during the training phase to supervise both the rigid transformation prediction and the prediction of σ_p . The loss function \mathcal{L}_s is divided into two parts: \mathcal{L}_q for supervising the rigid transformation prediction, and \mathcal{L}_σ for supervising the prediction of σ_p . Specifically, \mathcal{L}_σ is

represented by the cross-entropy loss between the predicted vector and the target vector (which is a vector of ones), while \mathcal{L}_q is represented by the point cloud reconstruction loss, weighted by σ_p . Since the network’s weights are optimized in the direction that minimizes the loss function during training, for correctly paired point pairs, the correct global rigid transformation prediction reduces \mathcal{L}_q , while for incorrectly paired point pairs, predicting a smaller σ_p reduces \mathcal{L}_q . At this point, σ_p can be used to represent the pairing score of point pairs. To avoid the model minimizing \mathcal{L}_q by predicting small (or even all-zero) σ_p for all point pairs, we introduce \mathcal{L}_σ , which calculates the loss with a vector of all ones. This encourages the predicted σ_p to approach 1, ensuring that for correctly paired point pairs, \mathcal{L}_q can only be minimized by predicting the correct global rigid transformation, thus avoiding a trivial solution where σ_p is extremely small or all-zero.

3.4 Loop-Closure Detection

The Loop-Closure Detection structure is shown in Figure 2, consisting of an Encoder, Decoder, and Decode Head. The Encoder and Decoder share the same structure as the Point Cloud Registration part, with weight sharing. The Decode Head follows the same strategy as DeepPointMap [33], where two weight-shared MLPs are stacked to predict the probability of a loop closure between the source point cloud and the target point cloud.

For the Encoder part, we adopt the PointNeXt [38] combined with CLI-GCN structure. Existing point cloud feature extraction methods (e.g., PointNet++ [24], VoxelNet [40], and the PointNeXt [25] used in this paper) aggregate local features through downsampling during the feature extraction process. Thus, although the final compressed descriptors contain rich semantic features, they suffer from issues such as single receptive field and low feature resolution, ignoring the importance of perceiving neighborhoods at different scales. For points in overlapping regions, changes in the size of neighborhood structures do not affect their similarity, while for points at the edges of overlapping regions, the similarity of neighborhood structures decreases sharply as the receptive field increases. This reduction in similarity of overlapping regions caused by low resolution may lead to incorrect loop closure predictions, introducing errors in robot localization and map construction. To address this, we construct the CLI-GCN module to perceive neighborhood structures of different scale sizes and capture richer geometric features.

The CLI-GCN structure is shown in Figure 4, consisting of two parts: (a) Cross-Layer Feature Point Sample: This part samples the deep feature points within shallow feature points based on distance; (b) Intra-Graph Convolution: Based on the sampling results, a local neighborhood graph is constructed and feature integration is performed.

Cross-Layer Feature Point Sample: The Cross-Layer Feature Point Sample structure is shown in Figure 4(a), and is mainly responsible for performing neighborhood

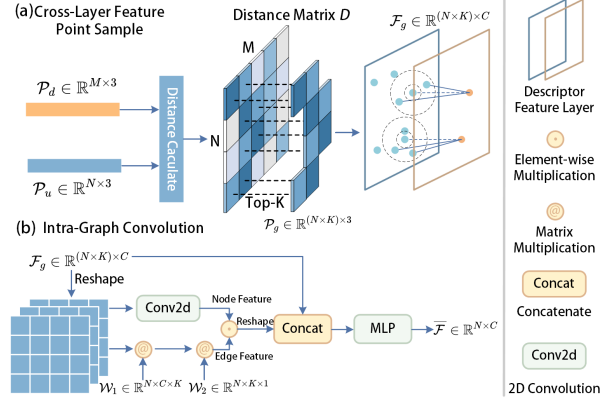


Figure 4: Overview of CLI-GCN. (a) is the overview of Cross-Layer Feature Point Sample; (b) is the the overview of Intra-Graph Convolution.

sampling of deep feature points within shallow feature points based on distance. Specifically, given a point cloud \mathcal{P} , the feature extraction is first performed using PointNeXt to obtain dense but small receptive field shallow features and sparse but large receptive field deep features (where $\mathcal{P}_d \in \mathbb{R}^{N \times 3}$ represents the 3D coordinates of the shallow features, i.e., the downsampling layer features in PointNeXt; $\mathcal{P}_u \in \mathbb{R}^{N \times 3}$ represents the 3D coordinates of the deep features, i.e., the upsampling layer features in PointNeXt). Then, the distance between each shallow feature point and each deep feature point is calculated based on \mathcal{P}_d and \mathcal{P}_u , resulting in an $M \times N$ distance matrix \mathcal{D} . Finally, for each row in the distance matrix, the K closest feature points are selected (with $K = 2$ as an example in Figure 4(a)), i.e., the K nearest shallow feature points to each deep feature point $\mathcal{F}_g \in \mathbb{R}^{(N \times K) \times C}$.

In addition, considering that we want the sampled feature points to describe the structural features of the current point cloud as much as possible, we avoid selecting feature points that are very close or overlap in 3D space with the deep feature points themselves. Therefore, two distance thresholds (in this paper, 0.5m and 1.0m) are set, prioritizing the selection of shallow feature points that are closest to the deep feature points within the threshold range. When the number of feature points within the threshold range is less than K , additional feature points outside the upper threshold are selected. We have visualized the deep feature points and the sampled local neighborhood graph feature points (as shown in Figure 5, where blue points represent the deep feature points, and orange points represent the sampled shallow feature points). It can be observed that the sampled local neighborhood graph feature points can more intuitively represent the local structure of the point cloud.

Intra-Graph Convolution: The structure of the Intra-Graph Convolution is shown in Figure 4(b). It mainly constructs a local neighborhood graph with \mathcal{F}_g and performs feature aggregation. The Intra-Graph Convolution

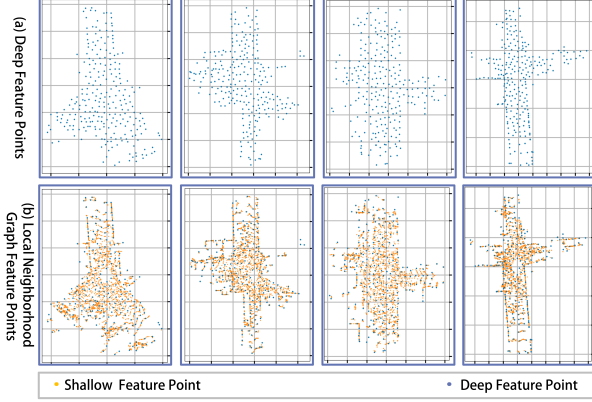


Figure 5: Visualization results of deep feature points and sampled local neighborhood graph feature points. The yellow point denotes the shallow feature point; the blue point denotes the deep feature point.

consists of two branches: the edge feature branch and the node feature branch. The edge feature branch is used to generate edge features for the local neighborhood graph, while the node feature branch is used to generate node features for the local neighborhood graph.

For the node feature branch, \mathcal{F}_g is first reconstructed into a 2D matrix $\mathcal{F}'_g \in \mathbb{R}^{N \times K \times C}$ (where C represents the feature dimension). After reconstruction, each row represents the neighborhood of a deep feature point, and the features within each row represent the shallow features within the neighborhood. Then, a 2D convolution is used to extract features and generate node features. It is important to note that, in the neighborhood graph we aim to generate, each deep feature point's neighborhood is independent to avoid interference between the node features of different deep feature points' neighborhoods during feature aggregation, which could affect the representation of local structural features. Therefore, a 2D convolution with a kernel size of 1×3 is used for feature aggregation, ensuring that only features within the same row interact, avoiding interference between different neighborhoods.

For the edge feature branch, two learnable weight matrices are used to integrate \mathcal{F}_g into edge features. Specifically, after reconstructing c into \mathcal{F}'_g , it undergoes matrix multiplication with two learnable weight matrices $\mathcal{W}_1 \in \mathbb{R}^{N \times C \times K}$ and $\mathcal{W}_2 \in \mathbb{R}^{N \times K \times 1}$ to obtain edge point features $\mathcal{F}_e \in \mathbb{R}^{N \times K \times 1}$, which represent the correlation between the shallow feature points in each neighborhood and their corresponding deep feature points. Finally, the node features and edge features are multiplied element-wise and concatenated with \mathcal{F}_g . This is followed by an MLP for the final feature aggregation to obtain $\bar{\mathcal{F}}_{dst} \in \mathbb{R}^{N \times C}$ (the mathematical formulation is given in (9)).

$$\bar{\mathcal{F}} = MLP \left(Cat \left(Reshape \left(\mathcal{F}'_g @ \mathcal{W}_1 @ \mathcal{W}_2 \right) \cdot \mathcal{F}_n, \mathcal{F}_g \right) \right) \quad (9)$$

where $MLP(\cdot)$ denotes the Multi-Layer Perceptron; $@$ denotes matrix multiplication; \mathcal{F}_n represents the node features; $Cat(\cdot)$ denotes the Concatenate operation; and $Reshape(\cdot)$ denotes the Reshape operation.

3.5 Loss Function

The training process is divided into two stages: the point cloud registration training stage and the loop-closure detection training stage. In the point cloud registration training stage, an end-to-end multi-task joint training strategy is used for training. The loss function consists of the following components: (1) Coarse Pairing Loss; (2) Pairing Loss; (3) Offset Loss; (4) Dynamic Segmentation Loss; (5) Importance Scoring Loss; (6) Loop-Closure Detection Loss.

Given $[p_i^{src}, f_i^{src}] \in [\hat{\mathcal{P}}_{src}, \hat{\mathcal{F}}_{src}]$ and $[p_j^{dst}, f_j^{dst}] \in [\hat{\mathcal{P}}_{dst}, \hat{\mathcal{F}}_{dst}]$, the paired samples are classified into positive samples \mathcal{Q}_+ , neutral samples \mathcal{Q}_o , and negative samples \mathcal{Q}_- .

$$\mathcal{Q}_+ = \left\{ (p_i^{src}, p_j^{dst}) \mid \arg \min_j \|p_i^{src} - p_j^{dst}\|_2, \right. \\ \left. \|p_i^{src} - p_j^{dst}\|_2 \leq \varepsilon_{positive} \right\} \quad (10)$$

$$\mathcal{Q}_o = \left\{ (p_i^{src}, p_j^{dst}) \mid \|p_i^{src} - p_j^{dst}\|_2 \leq \varepsilon_{positive} \right\} \quad (11)$$

$$\mathcal{Q}_- = \left\{ (p_i^{src}, p_j^{dst}) \mid \|p_i^{src} - p_j^{dst}\|_2 > \varepsilon_{positive} \right\} \quad (12)$$

where $\varepsilon_{positive}$ denotes the distance threshold, and the hyperparameter $\varepsilon_{positive} = 1m$.

Coarse Pairing Loss & Pairing Loss: We use the InfoNCE Loss [41], and its mathematical representation is as follows:

$$\mathcal{L}_c = -\log \left(\frac{\sum_{\mathcal{Q}_+} \exp \left(\hat{f}_i^{src} \odot \hat{f}_j^{dst} / \alpha \right)}{\sum_{\mathcal{Q}} \exp \left(\hat{f}_i^{src} \odot \hat{f}_j^{dst} / \alpha \right)} \right) \quad (13)$$

$$\mathcal{L}_p = -\log \left(\frac{\sum_{\mathcal{Q}_+} \exp \left(\hat{f}_i^{src} \odot \hat{f}_j^{dst} / \alpha \right)}{\sum_{\mathcal{Q}_+ \cup \mathcal{Q}_o} \exp \left(\hat{f}_i^{src} \odot \hat{f}_j^{dst} / \alpha \right)} \right) \quad (14)$$

where $\mathcal{Q} = \mathcal{Q}_+ \cup \mathcal{Q}_- \cup \mathcal{Q}_o$; the hyperparameter $\alpha = 0.2$.

Offset Loss: We follow the method in DeepPointMap, where the Mahalanobis distance is used to compute the Offset Loss. Its mathematical representation is as follows:

$$\mathcal{L}_o = \frac{1}{|\mathcal{Q}_+ \cup \mathcal{Q}_o|} \sum_{\mathcal{Q}_+ \cup \mathcal{Q}_o} \|\delta_{i,j} - \delta_{i,j}^*\|_{\Sigma} \quad (15)$$

where $\delta_{(i,j)}$ represents the offset predicted by the Offset Head; $\delta_{(i,j)}^*$ represents the ground-truth offset; and $\|\cdot\|_{\Sigma}$ denotes the Mahalanobis distance.

Importance Scoring Loss: \mathcal{L}_s is divided into \mathcal{L}_q , which supervises the prediction of q , and \mathcal{L}_{σ} which supervises

σ_p . Among them, \mathcal{L}_σ is represented by the binary cross-entropy with a ground-truth of all ones. The mathematical representation of \mathcal{L}_s is as follows:

$$\mathcal{L}_q = \frac{1}{|\mathcal{Q}_+ \cup \mathcal{Q}_o|} \sum_{\mathcal{Q}_+ \cup \mathcal{Q}_o} \sigma_p^{i,j} \left\| \frac{q}{\|q\|} p_i^{src} \left(\frac{q}{\|q\|} \right)^{-1} + \tilde{t} - p_j^{dst} \right\|_2 \quad (16)$$

$$\mathcal{L}_s = \lambda_q \mathcal{L}_q + \lambda_\sigma \mathcal{L}_\sigma \quad (17)$$

where the hyperparameter $\lambda_q, \lambda_\sigma = (0.5, 0.2)$; \tilde{t} denotes the translation component, and its data representation is as shown in (8).

Dynamic Segmentation Loss & Loop-Closure Detection Loss: We use cross-entropy to train the Dynamic Segmentation Head and the Loop-Closure Head. It is important to note that in the Loop-Closure training stage, the weights of the Encoder and Decoder parts are frozen, and only the Loop-Closure Detection Head is trained.

$$\mathcal{L}_{rg} = \lambda_1 \mathcal{L}_c + \lambda_2 \mathcal{L}_p + \lambda_3 \mathcal{L}_o + \lambda_4 \mathcal{L}_s + \lambda_5 \mathcal{L}_d \quad (18)$$

where the hyperparameter $\lambda_1, \lambda_2, \lambda_3, \lambda_4$, and λ_5 are 0.1, 1.0, 1.0, 1.0, and 1.0, respectively.

4 Experiments

4.1 Datasets

To evaluate the effectiveness of our method, we conducted experiments on the SemanticKITTI [42], KITTI-360 [43], and MulRan [44] datasets. In terms of quantitative evaluation, we adopted the APE (Absolute Pose Error), which is commonly used in the KITTI-360 benchmark, to assess the global accuracy of the predicted trajectories.

SemanticKITTI: SemanticKITTI [42] is a large outdoor open-source dataset based on the KITTI Vision Odometry Benchmark [45], which collects data from various scenarios, including urban traffic, residential areas, highways around Karlsruhe, Germany, and rural roads, using sensors such as onboard LiDAR and cameras. The original odometry data includes 22 sequences, of which we used 11 sequences (from sequence 00 to sequence 11) for the experiment. Sequence 00 to sequence 05 were used as the training set, and sequence 06 to sequence 10 were used as the test set.

KITTI-360: KITTI-360 [43] is a suburban driving dataset that uses 180° fisheye cameras, 90° front-facing cameras, as well as Velodyne HDL-64E and SICK LMS 200 LiDAR scanning units, providing accurate localization information. KITTI-360 consists of 11 large sequences (00, 01, 03-10, and 18). We used the first 6 sequences for training, and the rest for testing.

MulRan: MulRan [44] is a range dataset for urban location recognition and SLAM research, containing 12 sequences collected from 4 different environments. We used the

KAIST 03 (K03) and Riverside02 (R02) sequences as the test set, and all 6 sequences collected in Sejong and DCC as the training set.

4.2 Implementation Details

Data Augmentation: (1) Random Sampling: For each input point cloud frame, 16,384 points are randomly sampled. If the number of points in the input cloud is less than 16,384, zero-padding is applied. (2) Random Occlusion [33]: Random occlusion is applied in areas with an angular range of 10° to 150° and a distance range of 2m to 10m. n regions (up to 3 regions) are randomly occluded by removing all points passing through these regions, introducing an occlusion effect. (3) Random Rigid Transformation: The input point cloud undergoes random rigid transformations, where the rotation transformation is sampled from a uniform distribution with a mean of 0 and a standard deviation of 3.1416, and the translation transformation is sampled from a uniform distribution with a mean of 0 and a standard deviation of 3. (4) Random Local Map Registration: In practical SLAM tasks, the local map is typically constructed by registering the current frame’s point cloud with historical frames’ point clouds, with the local map expanding over time. Based on the distance to the current frame, we randomly sample 0 to n frames (where n gradually increases with each epoch, with n starting from 2 and doubling every 3 epochs, with a maximum value of 16) to construct the local map for registration as the target point cloud.

Training: The network is trained according to the following strategy, using the AdamW optimizer [51] with an initial learning rate of $lr = 10^{-3}$, weight decay $wd = 10^{-4}$, and a cosine learning rate scheduler [52]. The training is conducted on 3 RTX 3090 GPUs. For all tasks, the network is trained for 12 epochs, and the model from the final epoch is used for evaluation. Since only SemanticKITTI provides instantiated point cloud annotations, we trained the Dynamic Segmentation Head only on SemanticKITTI. For training on the KITTI-360 and MulRan datasets, we used the Dynamic Segmentation Head weights trained on SemanticKITTI and froze this part of the weights to prevent further training.

4.3 Compared with Others

To validate the effectiveness of our method, we conducted experiments on several datasets (SemanticKITTI, KITTI-360, and MulRan) and compared our results with seven state-of-the-art odometry and SLAM methods: KISSICP [50], LeGO-LOAM [21] and its follow-up work SC-LeGO-LOAM [46], Muls [47], CT-ICP [48], DeepPointMap [33], and the advanced point cloud registration method GeoTransformer [49].

Trajectory Estimated: The trajectory estimated: result of ADA-DPM on different datasets are shown in Figure 6, where the red line represents the ground-truth trajectory, the blue line represents the ADA-DPM predicted trajectory,

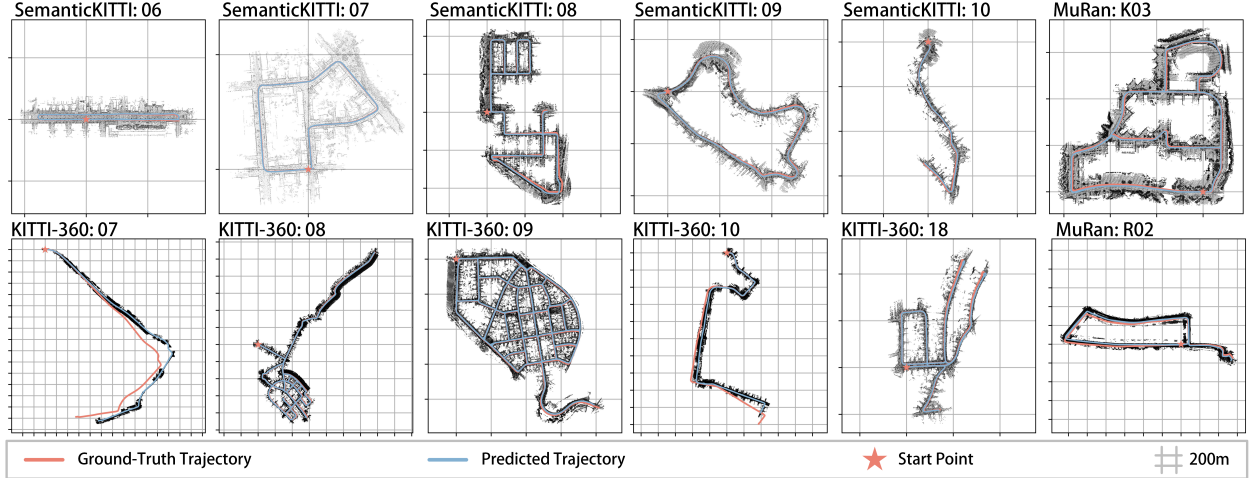


Figure 6: Trajectory estimated on different datasets. The blue line represents the predicted trajectory; the red line represents the ground-truth trajectory; the red pentagon represents the starting point; one grid represents 200m.

Table 1: Trajectory estimated results ($APE \downarrow$) on the test benchmarks. The **bold** indicates the best result, and the underline indicates the second-best result. GeoTransformer is a point cloud registration method, so for GeoTransformer, we perform end-to-end registration to complete the trajectory evaluation.

Method	SemanticKITTI					KITTI-360					MulRan	
	06	07	08	09	10	07	08	09	10	18	K03	R02
LeGO-LOAM [21]	0.88	0.67	8.84	1.95	1.37	82.84	32.79	7.36	26.56	2.80	-	-
SC-LeGO-LOAM [46]	1.02	1.46	6.23	8.31	1.69	47.78	8.47	22.38	9.57	6.27	3.85	28.16
MULLS [47]	0.48	0.38	4.16	1.99	0.97	47.25	8.24	93.88	11.99	1.52	6.63	-
CT-ICP [48]	0.56	0.43	4.07	<u>1.29</u>	0.94	14.43	-	11.41	7.11	-	-	-
GeoTransformer [49]	24.38	8.71	22.68	22.14	16.36	-	-	75.93	-	34.79	71.95	-
KISS-ICP [50]	0.61	0.35	3.58	1.32	0.94	<u>20.51</u>	26.24	24.00	8.75	2.22	12.85	27.16
DeepPointMap [33]	0.92	0.26	3.49	1.27	1.28	93.77	<u>5.21</u>	<u>1.02</u>	10.46	1.28	<u>1.73</u>	<u>15.67</u>
Ours	0.46	<u>0.31</u>	<u>3.79</u>	<u>1.29</u>	1.50	35.73	5.09	1.01	11.21	<u>1.48</u>	1.62	12.78

and the red pentagon marks the starting point of the trajectory. By comparing the predicted values with the ground truth, it can be observed that ADA-DPM performs well on the SemanticKITTI, KITTI-360, and MulRan datasets, achieving globally consistent map reconstruction. In particular, for long-range localization and mapping tasks like KITTI-360 (with sequences over 10,000 meters in KITTI-09), ADA-DPM performs admirably.

The comparison results of the 12 sequences on the test set benchmark with other algorithms are shown in Table 1. ADA-DPM achieved the best performance on 5 sequences and second-best performance on 3 sequences (since CT-ICP can only operate based on its own provided data, the results for CT-ICP are not shown on those sequences).

On one hand, ADA-DPM benefits from its deep learning-based feature encoding approach, which does not rely on distinctive reference objects, giving it good generalization capability across most scenarios (as can be seen in Table 1, some traditional methods struggle to generate accurate trajectories for sequences like Riverside02, which lacks obvious reference objects). On the other hand, for sequences

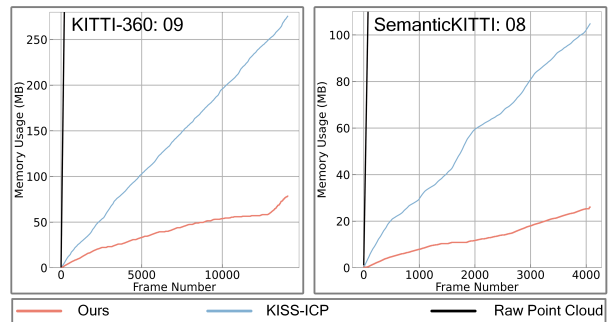


Figure 7: The memory consumption comparison with the map representation of KISS-ICP.

like KITTI-360 08 and 09, which contains many vehicles and pedestrians in urban roads, the Dynamic Segmentation Head effectively avoids interference from dynamic objects like vehicles and pedestrians. For suburban sequences with more vegetation, the Importance Scoring Head predicts the contribution of feature point pairs, emphasizing those

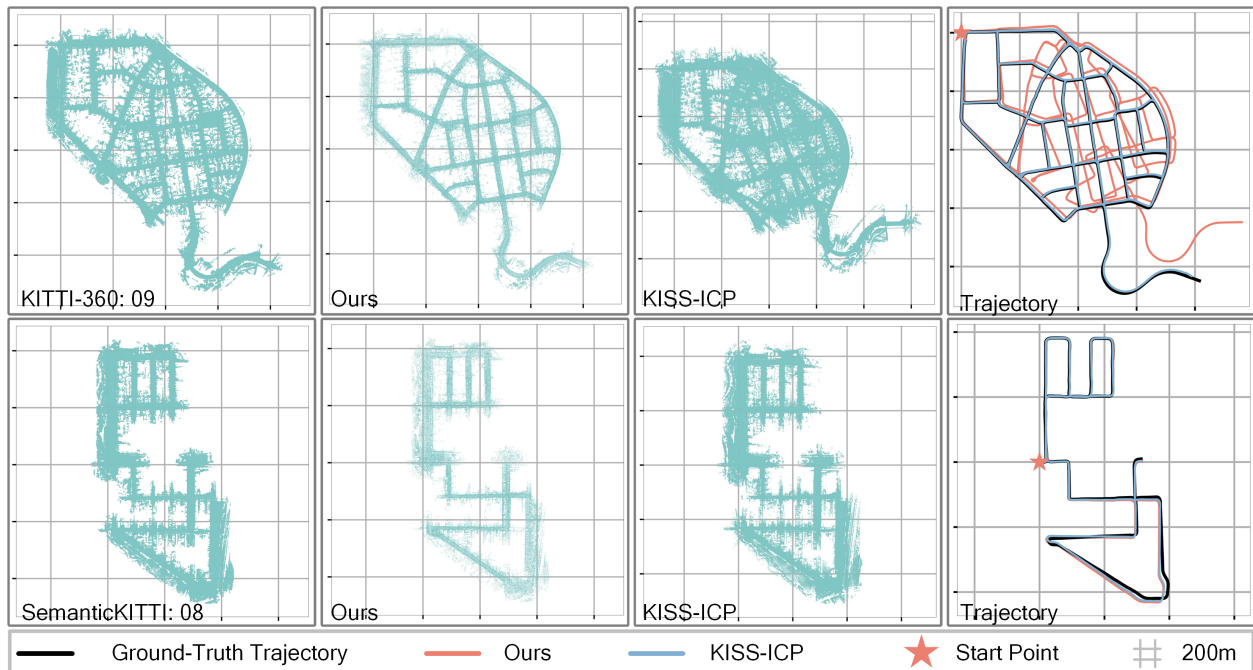


Figure 8: Visualization results of trajectory estimated and map reconstruction.

point pairs that contribute to registration (such as structural feature point pairs with regular geometric features) and filtering out non-structural feature point pairs (such as vegetation, which has irregular distribution).

Additionally, the Importance Scoring Head applies implicit supervision to the feature extraction network via global reconstruction loss, allowing the network to learn to extract feature points that contribute more to the point cloud registration task.

Finally, the GLI-GCN module alleviates the problem of reduced neighborhood structure similarity caused by a single receptive field, further improving localization and mapping accuracy in scenes with a high presence of loop closures (such as sequence 09 in KITTI-360).

Map Reconstruction: Efficient map representation is crucial for reconstructing large-scale maps. To evaluate the efficiency of our method in map reconstruction, we conducted further validation on two large sequences (SemanticKITTI:08 and KITTI-360:09). Specifically, we calculated the local storage data size of the map representations for our method and KISS-ICP (all data are stored in float32 data type). Figure 7 shows the memory consumption of different map representations in the two sequences. As illustrated in Figure 7, benefiting from the neural network-based sparse point cloud descriptors (we adopt the same map representation as DeepPointMap), compared with KISS-ICP, our method saves 60% memory in SemanticKITTI:07 and approximately 50% memory in KITTI-360 08.

Furthermore, to further evaluate the performance of our method in SLAM tasks, we visualized the predicted trajectories and reconstructed maps of our method and KISS-ICP on SemanticKITTI 08 and KITTI-360 09. The visualization is shown in Figure 8, where the first column is the ground-truth map, i.e., the global map reconstructed using ground-truth poses and the raw point cloud representation. The second and third columns are the map representations of our method and KISS-ICP, respectively, and the last column is the trajectories estimated by our method and KISS-ICP. It can be seen from the Figure 8 that compared with KISS-ICP, ADA-DPM can use less memory to construct a more accurate global map and has higher localization accuracy. Especially for the long-distance sequence KITTI-360 09, ADA-DPM achieves more accurate global consistent localization and mapping than KISS-ICP.

4.4 Ablation experiments

To further validate the effectiveness of each module in ADA-DPM, we conducted several ablation experiments. All experiments were performed on the same dataset split (we selected SemanticKITTI sequences 03-10 as the training sets and sequences 00-02 as the validation set).

We systematically removed the GLI-GCN module, Importance Scoring Head, and Dynamic Segmentation Head to evaluate their importance. Additionally, to further assess the generalization performance of the Importance Scoring Head in handling noisy points, we also compared the results under noise conditions. Specifically, we randomly apply Gaussian noise following a normal distribution $\mathcal{N}(0, 0.1^2)$ on 0% to 10% of the point cloud, and clip

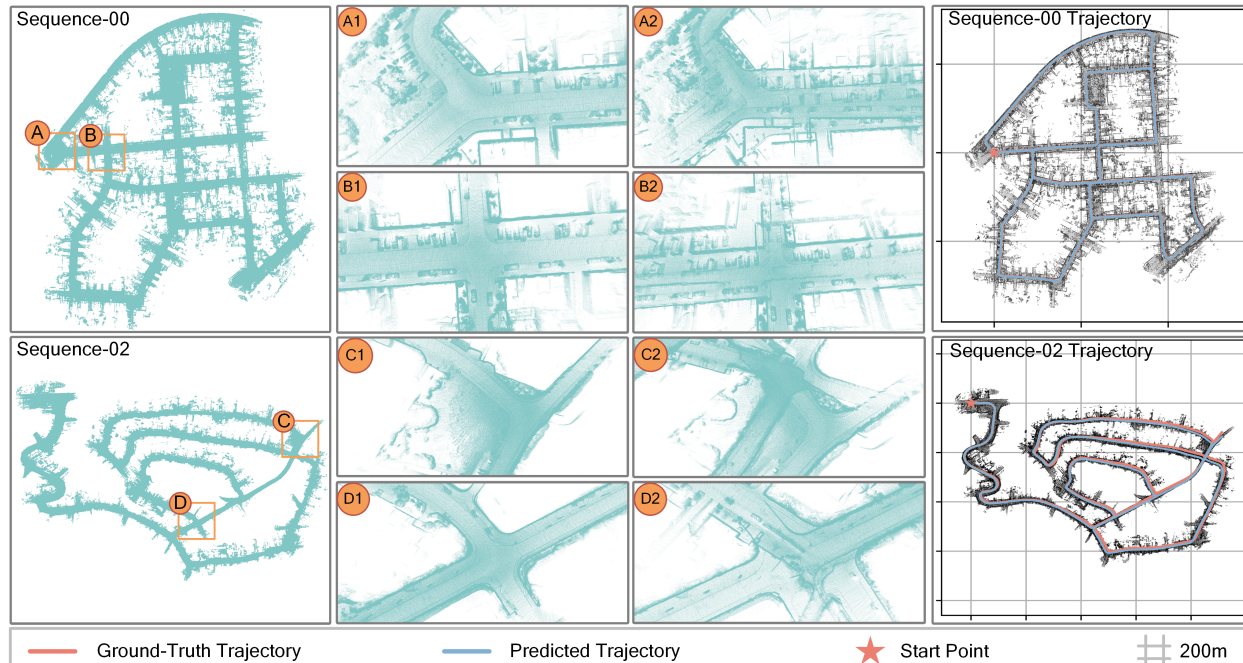


Figure 9: Global consistent dense mapping results on SemanticKITTI Sequence 00, 02. The blue line represents the predicted trajectory; the red line represents the ground-truth trajectory; the red pentagram represents the starting point.

Table 2: Trajectories estimated results ($APE \downarrow$) on the validation benchmark. The **bold** indicates the best result

Method	Dynamic Head	Scoring Head	GLI-GCN	Without Noise \ Noise		
				00	01	02
A				2.26\3.29	7.96\10.21	6.02\7.01
B	✓			2.01\2.72	8.52\10.82	5.21\7.44
C	✓	✓		2.64\2.84	6.16 \7.62	5.56\6.94
D	✓	✓	✓	0.91 \ 1.67	6.48\7.56	3.26 \4.32

Table 3: Trajectory estimation results ($APE \downarrow$) on the validation benchmark under different noise ratios.

Noise Ratio	SemanticKITTI			
	00	01	02	Mean
0 %	0.91	5.26	3.26	3.14
0–10 %	1.67	5.28	4.32	3.76 +19%
0–20 %	2.03	5.75	4.04	3.94 +25%
0–30 %	2.16	5.98	4.53	4.22 +34%
0–40 %	1.72	5.79	4.80	4.10 +30%
0–50 %	2.26	5.63	4.64	4.18 +33%

the noise on each axis to the range $[-0.1, 0.1]$. The experiment results are shown in Table 2. Where, method D refers to ADA-DPM; method C removes the GLI-GCN module based on method A; method B refers to removing the importance scoring head on the basis of method C; and method A removes the dynamic segmentation head from method B (i.e., the baseline method DeepPointMap).

By comparing method A with method B, we can observe that for urban scenes such as sequences 00 and 02 (scenes with more dynamic objects like vehicles and pedestrians), adding the Dynamic Segmentation Head helps to some extent eliminate the interference of dynamic objects. By comparing method B with method C, we find that, compared to method B, adding the Importance Scoring Head leads to an increase in error on sequences 00 and 02. After adding random noise, method C has a lower trajectory error than method D on sequence 01, while the performance difference on sequences 00 and 02 is minimal. The reason for this is that in loop-rich scenarios like sequences 00 and 02, loop closure detection can alleviate the cumulative errors caused by noise points to some extent, whereas in sequence 01, a loop-poor scenario, it is hard to mitigate cumulative errors through loop closure detection. However, method C, using the Importance Scoring Head to assign a contribution score to each feature point pair, can help mitigate the influence of noise points. Finally, by comparing method D with method C, we see that although the trajectory error in sequence 01 increases for method D, adding the GLI-GCN further improves the map-building accuracy in loop-rich areas like sequences 00 and 01.

Additionally, to further verify the generalization performance of ADA-DPM for noise points, we compared the test results under different numbers of noise points (with the maximum noise point ratios being 10%, 20%, 30%, 40%, and 50% respectively), and the test results are shown in Table 3. As can be seen from Table 3, even when noise is added to 50% of the point cloud, ADA-DPM can still complete the global consistent trajectory estimation.

Finally, to further verify the performance of the GLI-GCN module in areas with loop closures, we visualized the mapping results of ADA-DPM and ADA-DPM with the GLI-GCN module removed. The visualization results are shown in Figure 9. Where, A, B, C, and D represent four loop-closure positions, while A1, B1, C1, and D1 are the mapping results of ADA-DPM, and A2, B2, C2, and D2 are the mapping results of ADA-DPM with the GLI-GCN module removed. It can be observed that the maps constructed at each loop closure position exhibit consistent alignment. This successful alignment is attributed to the GLI-GCN, which utilizes different receptive fields from varying neighborhood sizes to generate local feature descriptors that fuse multiple receptive fields. This alleviates the issue of reduced neighborhood structural similarity in overlapping areas caused by a single receptive field, thereby further improving the localization and mapping accuracy in the overlapping regions.

5 Conclusions

In this paper, we address the challenges of dynamic objects, noise interference, and reduced similarity in overlapping regions due to low resolution in LiDAR SLAM for autonomous mobile robots, proposing an adaptive noise-filtering strategy—ADA-DPM.

Specifically, the Dynamic Segmentation Head is constructed to predict the probability of feature points being dynamic, filtering out moving objects to eliminate ego-motion interference. Secondly, the Importance Scoring Head assigns global contribution scores to feature point pairs, emphasizing reliable points for precise registration while discarding low-importance noise or unstructured points. Furthermore, to avoid trivial all-zero score predictions, we supervise the network with an importance score-weighted global reconstruction loss and a non-trivial scoring loss. Finally, the GLI-GCN module mitigates similarity degradation in overlapping regions caused by low resolution through cross-layer neighborhood graph construction, capturing richer geometric features to enhance loop closure accuracy.

Experimental results on multiple datasets demonstrate that ADA-DPM significantly improves robustness against dynamic objects and noise, outperforming state-of-the-art methods in challenging scenarios. The GLI-GCN module further enhances mapping accuracy in loop-rich environments by constructing local neighborhood features with abundant geometric information.

Notably, while ADA-DPM achieves promising performance in positioning accuracy and system robustness, neural network-based methods require more precise labeling (e.g., accurate robot poses), which is often insufficient in real-world SLAM applications, potentially affecting experimental outcomes. Our approach shows relatively weak performance in certain remote rural scenes (e.g., KITTI-360 07, 10), primarily due to sparse references and limited geometric information in point clouds.

References

- [1] B. Wang, Y. Wang, J. Huang, Y. Zeng, X. Liu, and K. Zhou, “Computed torque control and force analysis for mechanical leg with variable rotation axis powered by servo pneumatic muscle,” *ISA Transactions*, vol. 140, pp. 385–401, 2023.
- [2] Y. Shao, Z. Sun, A. Tan, and T. Yan, “Efficient three-dimensional point cloud object detection based on improved complex-yolo,” *Frontiers in Neurorobotics*, vol. 17, pp. 1 092 564–1 092 569, 2023.
- [3] Y. Shao, A. Tan, Z. Sun, E. Zheng, T. Yan, and P. Liao, “Pv-ssd: A multi-modal point cloud 3d object detector based on projection features and voxel features,” *IEEE Transactions on Emerging Topics in Computational Intelligence*, vol. 8, no. 5, pp. 3436–3449, 2024.
- [4] Y. Shao, A. Tan, B. Wang, T. Yan, Z. Sun, Y. Zhang, and J. Liu, “Ms23d: A 3d object detection method using multi-scale semantic feature points to construct 3d feature layer,” *Neural Networks*, vol. 179, pp. 106 623–106 637, 2024.
- [5] Z. Wang, L. Zhang, and H. Wang, “S2KAN-SLAM: Elastic neural lidar slam with sdf submaps and kolmogorov-arnold networks,” *IEEE Transactions on Circuits and Systems for Video Technology*, pp. 1–13, 2025.
- [6] X. Hu, Y. Wu, M. Zhao *et al.*, “DYO-SLAM: Visual localization and object mapping in dynamic scenes,” *IEEE Transactions on Circuits and Systems for Video Technology*, pp. 1–16, 2025.
- [7] H. Qi, X. Chen, Z. Yu *et al.*, “Semantic-independent dynamic slam based on geometric re-clustering and optical flow residuals,” *IEEE Transactions on Circuits and Systems for Video Technology*, vol. 35, no. 3, pp. 2244–2259, 2025.
- [8] Z. Hong, B. Wang, H. Duan *et al.*, “SP-SLAM: Neural real-time dense slam with scene priors,” *IEEE Transactions on Circuits and Systems for Video Technology*, pp. 1–13, 2025.
- [9] L. Guan and X. Yuan, “Dynamic weighting and boundary-aware active domain adaptation for semantic segmentation in autonomous driving environment,” *IEEE Transactions on Intelligent Transportation Systems*, 2024.
- [10] —, “Instance segmentation model evaluation and rapid deployment for autonomous driving using domain differences,” *IEEE Transactions on Intelligent Transportation Systems*, vol. 24, no. 4, pp. 4050–4059, 2023.
- [11] X. Shao, L. Zhang, T. Zhang *et al.*, “MOFISSLAM: A multi-object semantic slam system with front-view, inertial, and surround-view sensors for indoor parking,” *IEEE Transactions on Circuits and Systems for Video Technology*, vol. 32, no. 7, pp. 4788–4803, 2022.

- [12] J. Yang, H. Li, and Y. Jia, “Go-ICP: Solving 3d registration efficiently and globally optimally,” in *Proceedings of the IEEE International Conference on Computer Vision*, 2013, pp. 1457–1464.
- [13] A. Censi, “An icp variant using a point-to-line metric,” in *2008 IEEE International Conference on Robotics and Automation*, 2008, pp. 19–25.
- [14] J.-E. Deschaud, “IMLS-SLAM: Scan-to-model matching based on 3d data,” in *2018 IEEE International Conference on Robotics and Automation (ICRA)*, 2018, pp. 2480–2485.
- [15] Y. Li and T. Harada, “Lepard: Learning partial point cloud matching in rigid and deformable scenes,” in *Proceedings of the IEEE/CVF Conference on Computer Vision and Pattern Recognition*, 2022, pp. 5554–5564.
- [16] H. Xu, S. Liu, G. Wang *et al.*, “Omnet: Learning overlapping mask for partial-to-partial point cloud registration,” in *Proceedings of the IEEE/CVF International Conference on Computer Vision*, 2021, pp. 3132–3141.
- [17] Z. Liu, Y. Wang, S. Vaidya *et al.*, “KAN: Kolmogorov-arnold networks,” arXiv preprint, 2024, available: <https://arxiv.org/abs/2404.19756>.
- [18] P. J. Besl and N. D. McKay, “Method for registration of 3-d shapes,” in *Sensor Fusion IV: Control Paradigms and Data Structures*, vol. 1611. SPIE, 1992, pp. 586–606.
- [19] A. Segal, D. Haehnel, and S. Thrun, “Generalized-icp,” in *Robotics: Science and Systems*, vol. 5, 2009, p. 435.
- [20] J. Zhang and S. Singh, “LOAM: Lidar odometry and mapping in real-time,” in *Robotics: Science and Systems*, 2014, pp. 1–9.
- [21] T. Shan and B. Englot, “Lego-loam: Lightweight and ground-optimized lidar odometry and mapping on variable terrain,” in *2018 IEEE/RSJ International Conference on Intelligent Robots and Systems (IROS)*, 2018, pp. 4758–4765.
- [22] J. Lin and F. Zhang, “Loam livox: A fast, robust, high-precision lidar odometry and mapping package for lidars of small fov,” in *2020 IEEE International Conference on Robotics and Automation (ICRA)*, 2020, pp. 3126–3131.
- [23] W. Xu and F. Zhang, “Fast-lio: A fast, robust lidar-inertial odometry package by tightly-coupled iterated kalman filter,” *IEEE Robotics and Automation Letters*, vol. 6, no. 2, pp. 3317–3324, 2021.
- [24] C. R. Qi, H. Su, K. Mo *et al.*, “Pointnet: Deep learning on point sets for 3d classification and segmentation,” in *Proceedings of the IEEE Conference on Computer Vision and Pattern Recognition*, 2017, pp. 652–660.
- [25] C. R. Qi, L. Yi, H. Su *et al.*, “Pointnet++: Deep hierarchical feature learning on point sets in a metric space,” in *Advances in Neural Information Processing Systems*, 2017, pp. 1–10.
- [26] Z. J. Yew and G. H. Lee, “RPM-net: Robust point matching using learned features,” in *Proceedings of the IEEE/CVF Conference on Computer Vision and Pattern Recognition*, 2020, pp. 11 824–11 833.
- [27] J. Li, C. Zhang, Z. Xu *et al.*, “Iterative distance-aware similarity matrix convolution with mutual-supervised point elimination for efficient point cloud registration,” in *Computer Vision—ECCV 2020: 16th European Conference, Glasgow, UK, August 23–28, 2020, Proceedings, Part XXIV 16*. Springer, 2020, pp. 378–394.
- [28] K. Fu, S. Liu, X. Luo *et al.*, “Robust point cloud registration framework based on deep graph matching,” in *Proceedings of the IEEE/CVF Conference on Computer Vision and Pattern Recognition*, 2021, pp. 8893–8902.
- [29] Y. Aoki, H. Goforth, R. A. Srivatsan *et al.*, “Pointnetlk: Robust & efficient point cloud registration using pointnet,” in *Proceedings of the IEEE/CVF Conference on Computer Vision and Pattern Recognition*, 2019, pp. 7163–7172.
- [30] Z. J. Yew and G. H. Lee, “Regtr: End-to-end point cloud correspondences with transformers,” in *Proceedings of the IEEE/CVF Conference on Computer Vision and Pattern Recognition*, 2022, pp. 6677–6686.
- [31] Z. Chen, H. Chen, L. Gong *et al.*, “UTOPIC: Uncertainty-aware overlap prediction network for partial point cloud registration,” *Computer Graphics Forum*, vol. 41, no. 1. Wiley Online Library, 2022, pp. 87–98.
- [32] H. Xu, N. Ye, G. Liu *et al.*, “FINet: Dual branches feature interaction for partial-to-partial point cloud registration,” in *Proceedings of the AAAI Conference on Artificial Intelligence*, vol. 36, 2022, pp. 2848–2856.
- [33] X. Zhang, Z. Ding, Q. Jing *et al.*, “DeepPointMap: Advancing lidar slam with unified neural descriptors,” in *Proceedings of the AAAI Conference on Artificial Intelligence*, vol. 38, 2024, pp. 10 413–10 421.
- [34] P. Ruchti and W. Burgard, “Mapping with dynamic-object probabilities calculated from single 3d range scans,” in *2018 IEEE International Conference on Robotics and Automation (ICRA)*, 2018, pp. 6331–6336.
- [35] A. Milioto, I. Vizzo, J. Behley *et al.*, “RangeNet++: Fast and accurate lidar semantic segmentation,” in *2019 IEEE/RSJ International Conference on Intelligent Robots and Systems (IROS)*, 2019, pp. 4213–4220.
- [36] P. Pfreundschuh, H. F. Hendriks, V. Reijgwart *et al.*, “Dynamic object aware lidar slam based on automatic

- generation of training data,” in *2021 IEEE International Conference on Robotics and Automation (ICRA)*, 2021, pp. 11 641–11 647.
- [37] Q.-Y. Zhou, J. Park, and V. Koltun, “Open3D: A modern library for 3d data processing,” arXiv preprint, 2018, available: <https://arxiv.org/abs/1801.09847>.
- [38] G. Qian, Y. Li, H. Peng *et al.*, “Pointnext: Revisiting pointnet++ with improved training and scaling strategies,” in *Advances in Neural Information Processing Systems*, vol. 35, 2022, pp. 23 192–23 204.
- [39] V. Sitzmann, J. Martel, A. Bergman *et al.*, “Implicit neural representations with periodic activation functions,” in *Advances in Neural Information Processing Systems*, vol. 33, 2020, pp. 7462–7473.
- [40] Y. Zhou and O. Tuzel, “Voxelnet: End-to-end learning for point cloud based 3d object detection,” in *Proceedings of the IEEE Conference on Computer Vision and Pattern Recognition*, 2018, pp. 4490–4499.
- [41] A. V. D. Oord, Y. Li, and O. Vinyals, “Representation learning with contrastive predictive coding,” arXiv preprint, 2018, available: <https://arxiv.org/abs/1807.03748>.
- [42] J. Behley, M. Garbade, A. Milioto, J. Quenzel, S. Behnke, C. Stachniss, and J. Gall, “SemanticKITTI: A dataset for semantic scene understanding of lidar sequences,” in *Proceedings of the IEEE/CVF International Conference on Computer Vision*, 2019, pp. 9297–9307.
- [43] Y. Liao, J. Xie, and A. Geiger, “KITTI-360: A novel dataset and benchmarks for urban scene understanding in 2d and 3d,” *IEEE Transactions on Pattern Analysis and Machine Intelligence*, vol. 45, no. 3, pp. 3292–3310, 2022.
- [44] G. Kim, Y. S. Park, Y. Cho *et al.*, “Mulran: Multimodal range dataset for urban place recognition,” in *2020 IEEE International Conference on Robotics and Automation (ICRA)*, 2020, pp. 6246–6253.
- [45] A. Geiger, P. Lenz, and R. Urtasun, “Are we ready for autonomous driving? the KITTI vision benchmark suite,” in *2012 IEEE Conference on Computer Vision and Pattern Recognition*, 2012, pp. 3354–3361.
- [46] G. Kim, S. Choi, and A. Kim, “Scan context++: Structural place recognition robust to rotation and lateral variations in urban environments,” *IEEE Transactions on Robotics*, vol. 38, no. 3, pp. 1856–1874, 2021.
- [47] Y. Pan, P. Xiao, Y. He *et al.*, “MULLS: Versatile lidar slam via multi-metric linear least square,” in *2021 IEEE International Conference on Robotics and Automation (ICRA)*, 2021, pp. 11 633–11 640.
- [48] P. Dellenbach, J.-E. Deschaud, B. Jacquet *et al.*, “CT-ICP: Real-time elastic lidar odometry with loop closure,” in *2022 International Conference on Robotics and Automation (ICRA)*, 2022, pp. 5580–5586.
- [49] Z. Qin, H. Yu, C. Wang *et al.*, “Geotransformer: Fast and robust point cloud registration with geometric transformer,” *IEEE Transactions on Pattern Analysis and Machine Intelligence*, vol. 45, no. 8, pp. 9806–9821, 2023.
- [50] I. Vizzo, T. Guadagnino, B. Mersch *et al.*, “KISS-ICP: In defense of point-to-point icp—simple, accurate, and robust registration if done the right way,” *IEEE Robotics and Automation Letters*, vol. 8, no. 2, pp. 1029–1036, 2023.
- [51] S. J. Reddi, S. Kale, and S. Kumar, “On the convergence of adam and beyond,” in *International Conference on Learning Representations*, 2019.
- [52] L. N. Smith and N. Topin, “Super-convergence: Very fast training of neural networks using large learning rates,” in *Artificial Intelligence and Machine Learning for Multi-Domain Operations Applications*, vol. 11006. SPIE, 2019, pp. 369–386.